Rheo-Raman Spectroscopic Study on Uniaxial Deformation Behavior of High-Density Polyethylene Solids with Various Molecular Weight Distributions

Rheo-Raman Spectroscopic Study on Uniaxial Deformation Behavior of High-Density Polyethylene Solids with Various Molecular Weight Distributions

Takumitsu Kida, Yusuke Hiejima*, Koh-hei Nitta

Department of Chemical and Materials Science, Kanazawa University

Kakuma Campus, Kanazawa 920-1192, Japan

Abstract

The influences of the polydispersity index (M_w/M_n) on the morphology and deformation behavior of high-density polyethylene solids under uniaxial stretching were investigated using *in situ* Raman spectroscopy. An increase in M_w/M_n led to a larger fraction of tie molecules connecting several lamellar crystals, whereas no obvious influence on the crystalline structures was observed. Although the stress–strain curves essentially remained unchanged up to the neck-propagation region irrespective of M_w/M_n, the strain-hardening modulus was higher for higher M_w/M_n samples. These results indicate that the mechanical response of the network structure appears in the strain-hardening region because of the tie molecules connecting several lamellar crystals fragmented at the yield point. In addition, the molecular orientation of the crystalline chains into the stretching direction and the formation of long consecutive trans chains were enhanced for higher M_w/M_n samples.

1. Introduction

Semi-crystalline polymers such as polyethylene (PE) and polypropylene (PP) exhibit a spherulitic structure, which is the most typical supermolecular structure of melt-crystallized structures, where the lamellar crystals consisting of folded molecular chains radiate from its center.[1,2] Amorphous layers are present in the interlamellar regions in the form of ties, loops, cilia, and floating chains.[3,4] The tensile properties of these spherulitic polymer solids are dominated by various levels of hierarchy in the structure such as the crystalline thickness, the structural organization in the residual amorphous region, and the gross spherulitic morphology.[5-7] These structural variables are controlled by the molecular morphology, which depends directly on the molecular constitution (including the molecular weight and its polydispersity) as well as on external preparation conditions such as the cooling temperature and pressure. These dependences are observed because the molecular mobility and self-diffusion coefficient under crystallization are governed by the molecular constitution and external conditions.[8-10] However, the influence of the molecular constitution on the mechanical properties of spherulitic PE and PP has not been well investigated as the diversity and independence of the structural variables make it difficult to clarify the influences of the molecular weight and its distribution on the tensile and deformation behavior.

The present work is restricted to high-density polyethylenes (HDPEs) which are some of the most widely used polymers, with the expectation of further expansion of their applications in the future. The objective of this study was to explore the influences of the molecular weight distribution of HDPE on the stress–strain behavior. The HDPE polymers studied were binary blends of two HDPEs with a similar molecular mass and different molecular weight distributions in such a manner that the weight-averaged molecular weight was fixed as much as possible. In addition, their structural variables such as the crystalline and amorphous layer thicknesses, which are core elements of the structural morphology in semi-crystalline polymer solids, were fixed.

Uniaxial deformation behavior of semi-crystalline polymers has been extensively studies for elucidating the relationship between the microscopic structure and the mechanical properties.[1,11-14] Under the uniaxial stretching, the crystalline lamellae are fragmented into smaller lamellar blocks or lamellar cluster units followed by the reorientation of these blocks in the yielding region.[11,12] Thus, the mechanical response in the yielding region is mainly dominated by the lamellar crystalline structure. On the other hand, beyond the yielding point, the deformation of the crystalline structure is almost completed and the highly-oriented fibrillar structure is formed.[13,15,16] Therefore, the

stretching of tie chains connecting the adjacent lamellar crystals and entangled amorphous chains is the dominant deformation process in the strain-hardening region.[17,18]

Spectroscopic techniques are powerful tools that can be used to elucidate the microscopic deformation behaviors such as the molecular orientation, molecular conformation, and load applied on the molecular chains for various polymeric materials.[19] *In situ* small-angle X-ray scattering (SAXS) and wide-angle X-ray diffraction (WAXD) measurements have been intensively used for investigating microscopic structural changes during deformation in semi-crystalline polymers. The orientation behavior of the alternate lamellar structure has also been examined using SAXS measurements under tension.[20-22] WAXD measurements provide information on the crystallinity and crystalline form.[23-25] Infrared (IR) spectroscopy has been also used to examine the microscopic deformation behavior, such as the molecular orientation, in both crystalline and amorphous phases.[26-29]

Raman spectroscopy is a vibrational spectroscopy approach that has been applied to investigate microscopic deformation and structural changes in polymeric materials.[19,30,31] For polyolefins, the molecular orientation of the skeletal chains can be directly detected because the C–C stretching modes are strongly Raman active. Moreover, two orientation parameters are obtained from the polarized Raman spectra, giving the distribution of the molecular orientation.[32,33] Raman spectroscopy enables us to quantitatively analyze the sample morphology because the intensities of the Raman bands are very sensitive to

conformational changes.[34-37] In previous works, we developed an *in situ* Raman spectroscopic system and investigated the microscopic deformation behavior under uniaxial stretching.[38-40] In the present work, we investigated the molecular aspect of the tensile properties of HDPE polymers with different molecular weight distributions under tension using *in situ* Raman spectroscopy.

2. Experimental

2.1 Sample preparation

Two HDPE samples, HDPE-A ($M_w = 1.53 \times 10^5$, $M_w/M_n = 6.3$) and HDPE-D ($M_w = 1.68 \times 10^5$, $M_w/M_n = 34.4$), supplied by Japan Polychem Corporation were used in this study. It was confirmed from IR spectra that the present HDPE samples contain essentially no short-chain branches. HDPE samples with similar M_w values were chosen. HDPE-A and HDPE-D were blended at 190°C and 50 rpm with weight fractions of 7:3 and 3:7 to give HDPE-B and HDPE-C, respectively. The characteristics of all of the samples are tabulated in Table 1. Note that HDPE-A and HDPE-D were also kneaded under the same conditions to exclude the effect of the kneading procedure. Sample sheets with 1-mm thickness were prepared using hot pressing at 210°C and 20 MPa for 5 min followed by quenching in ice water. The sample sheets were annealed at each temperature to tune the crystallinity to ~60%.

Table 1. Characteristics of HDPE samples.

Sample code	$M_w/10^5$	M_w/M_n	ω /wt.%	T_a/°C	χ_v/vol.%	L_p/nm	L_c/nm
HDPE-A	1.53	6.3	0	40	59	19.5	14.6
HDPE-B	1.56	11.7	30	60	60	19.2	14.5
HDPE-C	1.63	21.7	70	100	60	19.0	14.3
HDPE-D	1.68	34.4	100	110	59	19.2	14.6

ω: weight fraction of HDPE-D, T_a: annealing temperature, χ_v: volumetric crystallinity

L_p: long period, L_c: thickness of lamellar crystal

2.2 Measurements

Tensile tests were performed at a constant strain rate of 0.5 min^{-1} using a custom-made tensile machine at room temperature. Dumbbell-shaped specimens with a gauge length of 10 mm and width of 4 mm were cut from the sample sheets.

In situ Raman spectroscopy was performed to examine the real-time changes of the Raman spectra during the uniaxial stretching. The details of our *in situ* Raman spectroscopic system are described in previous publications.[38-41] Briefly, a custom-made small tensile tester with a double-drawing mechanism was installed in the Raman spectrometer and the laser light from a diode-pumped solid-state laser (RLK-640-200, LASOS, Jena, Germany) was used as the excitation light. The power and wavelength were 639.7 nm and 200 mW, respectively. The excitation light was monochromated with a laser line filter and irradiated the central portion of the specimen. Note that a double-

notch-shaped specimen (2-mm gauge length and 4-mm width) was used in this study; because of the small gauge length, the necking deformation always occurred at the center of the specimen. Thus, the laser light was irradiated the necked portion after yielding. The elongation speed and temperature were set to 1 mm min^{-1} and 20°C, respectively. The backward-scattered light was collected with a pair of convex lenses, and the Rayleigh scattered light was removed with a Raman long-pass filter. A charge-coupled device camera with a monochromator (PIXIS100 and SpectraPro 2300i, Princeton Instruments, Trenton, NJ) was used as the detector. To evaluate the molecular orientation, the polarization direction of the incident light was controlled by inserting a half-wavelength plate, and the scattered light was polarized with a wire-grid polarizer. The polarized Raman spectra were obtained in the *zz*, *zy*, and *yy* geometries, where *z* and *y* represent the polarization direction parallel and perpendicular to the stretching direction, respectively, and the first and second characters represent the polarization directions of the analyzer and polarizer, respectively. Polarization dependences of the spectrometer and the optics were corrected by using a polarization scrambler (DEQ-25, SIGMAKOKI Co., Ltd., Tokyo, Japan) and carbon tetrachloride, respectively.

Note that all of the mechanical tests including *in situ* Raman spectroscopy were performed at least 5 times for obtaining the standard deviations for all of the data.

3. Characterization

3.1 Molecular weight

High-temperature gel permeation chromatography (HT-GPC) was performed at 140°C using a Viscotek Triple Detector HT-GPC (Model-SG system, Malvern Instruments, Worcestershire, UK). *o*-dichlorobenzene with 0.05% butylated

hydroxytoluene as the anti-oxidant was used as the solvent. The HDPE samples were dissolved at a concentration of 1.0 mg ml^{-1}. A polystyrene (PS) standard sample was used for the column calibration. The molecular weights in terms of PS were converted to terms of PE using a calibration coefficient obtained from the GPC traces of PE standard samples (Polymer Laboratories Ltd., M_w: 800, 1214, 2306, 13600, 32100, and 119600, $M_w/M_n \sim 1.1$).

3.2 Structural characteristics

The volumetric crystallinity of each sample was estimated from the density determined using the Archimedes method, where the crystalline and amorphous densities were assumed to be $\rho_c = 1003$ kg m^{-3} and $\rho_a = 855$ kg m^{-3}, respectively.[42]

SAXS measurements were performed using a Nano-Viewer (Rigaku, Japan) with CuKα radiation (40 kV and 30 mA). Two-dimensional (2D) scattering patterns were obtained using an imaging plate with an exposure time of 30 min. The characteristic sizes of the lamellar structure (long period L_p and lamellar thickness L_c) were estimated from the normalized linear correlation function $g(r)$, which was calculated from the Fourier transform of the one-dimensional (1D) radial intensity distribution $I(q)$.[43] As shown in Table 1, L_p and L_c remained the same irrespective of M_w/M_n, indicating that the lamellar structures were essentially unaffected by M_w/M_n.

3.3 Probability of forming tie molecules

Tie molecules bridge the adjacent lamellar crystals in the amorphous layer between the lamellar crystals.[4] According to Huang and Brown[44], the probability that a

single molecular chain forms a tie molecule connecting n layers of the lamellar crystals is

$$f_t(n) = \frac{\int_{L(n)}^{\infty} r^2 \exp(-\beta r^2) dr}{3\int_0^{\infty} r^2 \exp(-\beta r^2) dr}, \quad (1)$$

where $L(n)$ is the minimum length required to form a tie molecule connecting n layers of the lamellar crystals represented using the crystalline (L_c) and amorphous (L_a) thicknesses:

$$L(n) = nL_c + (n-1)L_a. \quad (2)$$

Here, r is the end-to-end distance of the random coil in the melt and $\beta = 3/(2\bar{r}^2)$ is written as its root mean square value ($\bar{r}$). The value of $\bar{r}$ is represented by

$$\bar{r} = \left(\frac{C_N a^2 M}{M_0}\right)^{1/2}, \quad (3)$$

where C_N is the characteristic ratio, a is the bond length, M is the molecular weight of the polymer chain, and M_0 is the molar mass of the chain unit. For PE, $\bar{r}$ was calculated using the values of $C_N = 8.0$, $a = 0.154$ [nm], and $M_0 = 14$.[45] For a polymer, the molecular weight distribution should also be considered to calculate the tie-molecule fraction. Thus, the tie-molecule fraction as the probability of connecting n lamellae ($F_t(n)$) can be evaluated by averaging with the molecular weight distribution as

$$F_t(n) = \frac{\int_0^{\infty} f_n(M) f_t(n) dM}{\int_0^{\infty} f_n(M) dM}. \quad (4)$$

In this work, the number-averaged molecular weight distribution function $f_n(M)$ obtained from the GPC measurements was used.

3.4 Molecular orientation and conformation

In situ polarized Raman spectra for HDPE-D at $\varepsilon = 7$ are presented in Figure 1(a). The intensity of the Raman band at 1130 cm^{-1} assigned to the crystalline C–C

symmetric stretching mode shows a strong dependence on the polarization direction, indicating that the crystalline chains were highly oriented in the stretching direction (*z*-direction). Each Raman spectrum was fitted with a sum of Voigt functions using the nonlinear Levenberg–Marquardt method to determine the peak area, as shown in Figure 1(b). The fitting error of the peak area was less than ±2.0%.

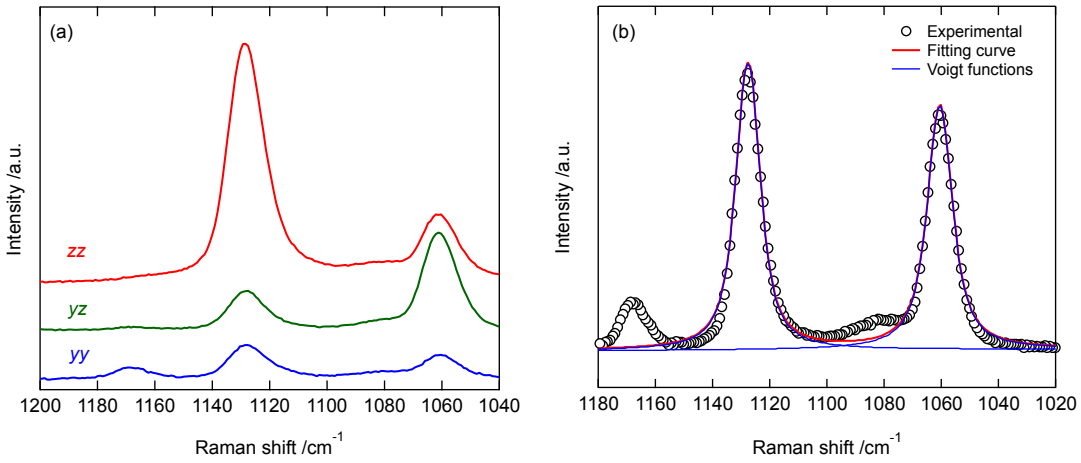

Figure 1. (a) Polarized Raman spectra of HDPE_D at $\varepsilon = 7$ and (b) non-polarized Raman spectrum of unstretched HDPE_D (circles). The red line represents the fitting curve from a sum of Voigt functions (blue lines).

The intensities of the Raman bands at 1130 cm^{-1} at various polarization geometries can be described by the following equations[32,33,46-48]:

$$I_{zz} = b\left\{\frac{1}{15}(8a^2 + 4a + 3) - \frac{4}{21}(4a^2 - a - 3)\langle P_2\rangle + \frac{8}{35}(a^2 - 2a + 1)\langle P_4\rangle\right\}, \quad (5)$$

$$I_{yy} = b\left\{\frac{1}{15}(8a^2 + 4a + 3) + \frac{2}{21}(4a^2 - a - 3)\langle P_2\rangle + \frac{3}{35}(a^2 - 2a + 1)\langle P_4\rangle\right\}, \quad (6)$$

$$I_{yy} = b\left\{\frac{1}{15}(a^2 - 2a + 1) + \frac{1}{21}(a^2 - 2a + 1)\langle P_2\rangle - \frac{4}{35}(a^2 - 2a + 1)\langle P_4\rangle\right\}, \quad (7)$$

where I_{ij} denotes the peak intensity for each polarization direction, and a and b are associated with the principal elements of the Raman tensor of the Raman bands at 1130

cm^{-1} for PE. The orientation parameters $\langle P_2 \rangle$ and $\langle P_4 \rangle$ are defined by the following equations[31]:

$$\langle P_2 \rangle = \frac{3\langle \cos^2 \theta \rangle - 1}{2}, \tag{8}$$

$$\langle P_4 \rangle = \frac{35\langle \cos^4 \theta \rangle - 30\langle \cos^2 \theta \rangle + 3}{8}, \tag{9}$$

where θ denotes the angle between the chain axis and stretching direction. Because Equations (5)–(7) include 4 unknown parameters ($\langle P_2 \rangle$, $\langle P_4 \rangle$, a and b), an auxiliary equation is required to calculate the values of orientation parameters. Recently, Richard-Lacroix and Pellerin proposed a new accurate method for calculating the values of orientation parameter $\langle P_2 \rangle$, namely most probable distribution (MPD) method, which is based on the most probable molecular orientation function.[48,49] Based on this method, $\langle P_4 \rangle$ in Equations (5)–(7) is replaced by the most probable value ($\langle P_4 \rangle_{mp}$) related to $\langle P_2 \rangle$ through the following equations (that consider maximization of the information entropy of the orientation distribution), so that Equations (5)–(7) are numerically solved for the three parameters, $\langle P_2 \rangle$, a, and b.

$$\langle P_4 \rangle_{mp} = -0.083\langle P_2 \rangle + 1.366\langle P_2 \rangle^2 - 1.899\langle P_2 \rangle^3 + 1.616\langle P_2 \rangle^4, \tag{10}$$

$$\langle P_4 \rangle_{mp} = 0.052\langle P_2 \rangle + 1.574\langle P_2 \rangle^2 + 3.968\langle P_2 \rangle^3 + 8.058\langle P_2 \rangle^4. \tag{11}$$

Equations (10) and (11) are used for the positive and negative $\langle P_2 \rangle$, respectively.

The Raman bands at 1063 and 1130 cm^{-1} are assigned to the C–C stretching modes of the long consecutive trans chains (10 or more consecutive trans bonds), and the mass fraction of the long consecutive trans chains for an undrawn specimen is described by[36,50]

$$\chi_t = \frac{I_{1130}}{0.89(I_{1298} + I_{1305})}, \tag{12}$$

where I_{1130}, I_{1298}, and I_{1305} are the peak intensities of the Raman bands at 1130, 1298, and 1305 cm^{-1}, respectively. The constant 0.89 was determined by Strobl and Hagedorn from the ratio of I_{1130} and $I_{1298}+I_{1305}$ for the highly-extended PE samples.[50] Although the fraction of the long consecutive trans chains can be obtained from the Raman bands at 1063 and 1130 cm^{-1}, the error in the intensity of the 1063 cm^{-1} band is appreciably larger than that of the 1130 cm^{-1} band because of the overlap by the amorphous band at 1080 cm^{-1}.

Because the sum of the peak intensities I_{1298} and I_{1305} is independent of the temperature[50], the sum is used as an internal reference. From the intensity of the 1418 cm^{-1} band assigned to the CH_2 bending mode in the orthorhombic crystal, the orthorhombic crystallinity can be written as[50]

$$\chi_c = \frac{I_{1418}}{0.46(I_{1298} + I_{1305})}. \tag{13}$$

Here, I_{1418} is the peak intensity of the 1418 cm^{-1} band.

For the drawn specimens, the intensities of the Raman bands whose Raman tensor belongs to the A_g symmetric group are strongly affected by the molecular orientation. Lagaron *et al.* proposed that the correction factor for the molecular orientation depends only on the symmetric group[51]. The Raman tensor symmetry of the Raman bands at 1063 and 1130 cm^{-1} are $B_{2g}+B_{3g}$ and A_g[52,53], respectively, and both of the bands are assigned to the long consecutive trans chains. Thus, the deviation of the ratio between these two band intensities from that of the undrawn specimen can be attributed to the effect of the molecular orientation:

$$\left(\frac{I_{1130}}{I_{1063}}\right)_{\text{undrawn}} = C(\varepsilon)\left(\frac{I_{1130}}{I_{1063}}\right)_{\text{drawn}}. \tag{14}$$

Here, $C(\varepsilon)$ is the correction factor of the molecular orientation. The strain dependence of the correction factor $C(\varepsilon)$ is shown in Figure S1 in the Supporting Information. If we assume that the Raman tensor of the 1305 cm^{-1} band has the B_{2g}+B_{3g} symmetry as same as the band at 1298 cm^{-1} (reported by Lagaron *et al.*)[51], the fraction of the long consecutive trans chains of the drawn specimens can be calculated using the following equation with the correction factor:

$$\chi_{\mathrm{t,drawn}} = C(\varepsilon)\frac{I_{1130}}{0.89(I_{1298} + I_{1305})}. \tag{15}$$

Moreover, the orthorhombic crystallinity of the drawn specimens can be represented by modifying Equation (13) as follows because the Raman tensor of 1418 cm^{-1} has the same A_g symmetry as that of the 1130 cm^{-1} band:

$$\chi_{\mathrm{c,drawn}} = C(\varepsilon)\frac{I_{1418}}{0.46(I_{1298} + I_{1305})}. \tag{16}$$

We confirmed that the corrected values given by Equations (15)–(16) are essentially unaffected by the angle between the polarization direction of the incident light and the stretching direction (see Figure S2 in the Supporting Information), suggesting that the present correction method eliminates any effects of the molecular orientation.

Raman spectra in the low-frequency ranges from −20 to −3.2 cm^{-1} and 3.2 to 100 cm^{-1} were measured using a double monochromator (Ramanor U1000, Jobin Yvon, Longjumeau, France). An Ar^+ ion laser (wavenumber = 488 nm, power = 50 mW) was used as the incident beam, and the backscattered geometry was employed. The Raman intensity was measured at 25°C with an exposure time of 2 s every 0.2 cm^{-1}. For semi-crystalline polymers, Raman bands assigned to the longitudinal acoustic mode (LAM) are observed in the low-frequency region (5–100 cm^{-1}), and the peak position of the LAM

band q is related to the length of the straight-chain segment (SCS) L_{SCS}, reflecting the lamellar thickness[54-57]:

$$q = \frac{1}{2cL_{SCS}}\sqrt{\frac{E_c}{\rho_c}}, \quad (17)$$

where L_{SCS} is the length of the SCSs, c is the speed of light, E_c is the crystalline modulus, and ρ_c is the crystalline density. For PE, L_{scs} was calculated using the values of E_c = 2.9×10^9 Pa[58] and ρ_c = 1003 kg m^{-3}. The dynamical susceptibility was determined by correcting the Bose–Einstein factor using the following equation[59]:

$$\chi''(\nu) = K(\nu_i - \nu)^{-3}[n(\nu) + 1]^{-1}I(\nu) \quad (18)$$

where $I(\nu)$ is the experimental Raman intensity, $n(\nu) = [\exp(hc\nu/kT)-1]^{-1}$ is the Bose–Einstein factor, ν_i is the frequency of incident laser light, K is the instrumental factor, T is temperature, and c is the light speed. Note that the Raman shift was calibrated by fitting the central Rayleigh scattering peak to a Gaussian curve.

4. Results and discussion

Figure 2 presents the GPC curves for the HDPE samples. The values of M_w and M_w/M_n determined from these GPC curves are presented in Table 1. The peak positions of the GPC curves remained almost constant as the M_w values were fixed to be approximately 1.6×10^4. Their width obviously expanded with increasing HDPE-D content, as the standard deviation of the molecular weight distribution is given by $M_n\sqrt{(M_w/M_n)^2 - 1}$. Thus, this set HDPE samples was suitable to examine the influence of the molecular distribution index M_w/M_n.

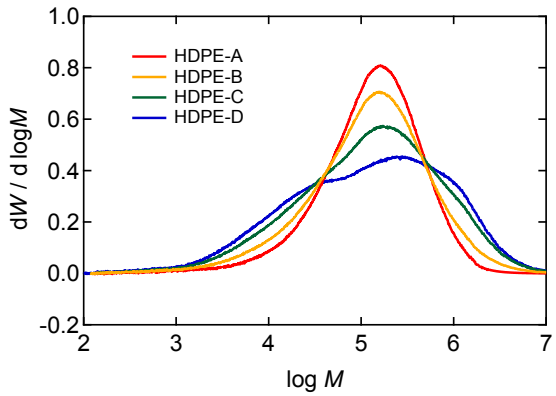

Figure 2. GPC curves of all the samples.

Figure 3(a) presents the Raman spectra in the lower-frequency regions for all the samples. A single low-frequency Raman band assigned to the LAM-1 of PE is observed at approximately 18 cm^{-1} for each sample. Although two LAM-1 bands are observed for HDPEs with a bimodal molecular weight distribution because of the bimodal distribution of the lamellar crystalline thickness[60], a single unimodal LAM-1 band was observed for the present HDPEs. This result suggests that the molecular chains were well mixed and that lamellar crystals with a unimodal distribution of thickness were formed. The length of the SCS, L_{SCS}, and the full width at half maximum (FWHM) of the SCS estimated from the spectra using Equation (17) are shown in Figure 3(b). The L_{SCS} and FWHM remained almost constant irrespective of M_w/M_n. Because the HDPE samples essentially had the same L_p and L_c, as shown in Table 1, it can be concluded that the lamellar morphology was not affected by M_w/M_n. Considering that all the samples had a similar M_w, the independence of M_w/M_n on the crystalline structure suggests that M_w is the core element of the morphology formation of the alternative lamellar structure and that the influence of the polydispersity is confined to the structural organization in the amorphous region.

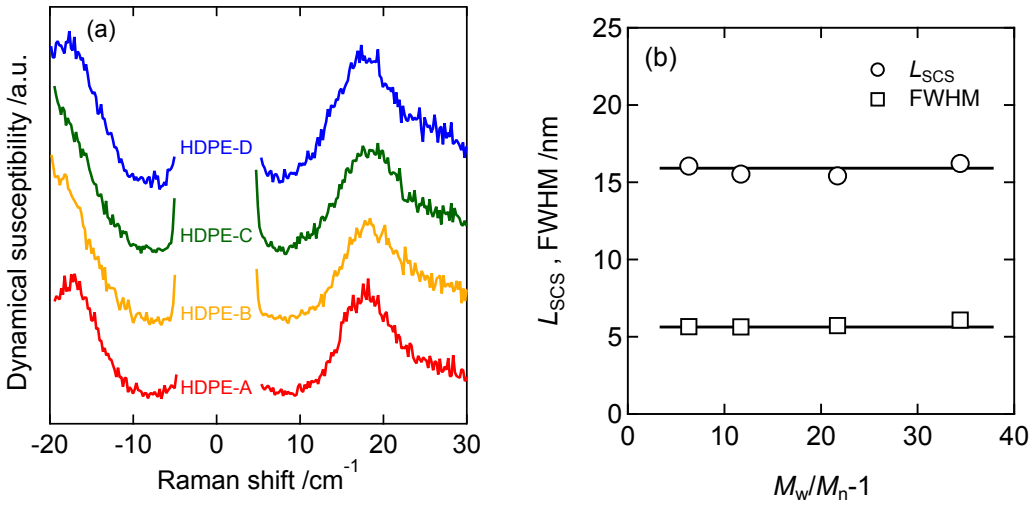

Figure 3. (a) Low-frequency Raman spectra of HDPE samples and (b) L_{SCS} and FWHM of L_{SCS} as a function of M_w/M_n.

Figure 4 shows the fractions of tie molecules connecting two, three, and four lamellar crystals, which were estimated from the GPC curves using Equation (4). The fraction of the tie molecules connecting two lamellar crystals is practically independent of M_w/M_n, whereas those of the tie molecules connecting three or four lamellar crystals show appreciable increases with increasing M_w/M_n. These results suggest that the presence of higher-molecular-weight components results in an increase in the fraction of tie molecules connecting several lamellar crystals.

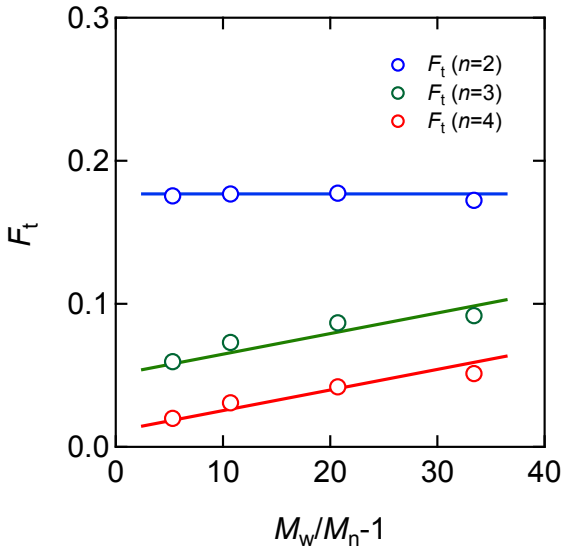

Figure 4. M_w/M_n dependence of the fractions of the tie molecules connecting two (blue), three (green), and four (red) lamellar crystals.

The stress–strain curves of all the HDPE samples are compared in Figure 5. The stress–strain curves of spherulitic HDPE samples are stepwise and can be divided into four zones.[1,61] In the initial strain region, the stress is almost proportional to the applied strain followed by the appearance of a maximum point on the nominal stress–strain curve. This maximum point, i.e., the yield point, is associated with the onset of temporal plastic deformation. Beyond the yield point, a concave contraction suddenly initiates on the specimen and coalesces into a well-defined neck, where the onset of permanent plastic deformation occurs.[62-64] The nominal stress remains constant until the necking boundaries propagate throughout the entire length of the specimen. During the necking process, a macroscopic morphological transformation from isotropic spherulitic to anisotropic fibril structures occurs accompanied by the fragmentation and/or rearrangement of parts of the stacked crystalline lamellae.[1,12,62,65] The extension ratio in the neck-propagation region is generally defined as the natural draw ratio λ_{ND}.[66,67] After necking, an upsweep in the

stress–strain curve, termed strain hardening, occurs, and the stress continues to increase up to the break point.

As shown in Figure 5, although the stress–strain curves of the HDPE samples were essentially identical in the elastic, yielding, and neck-propagation regions, the slope of the strain-hardening region obviously increased with increasing M_w/M_n. Considering that the lamellar crystalline morphology was unchanged for these HDPEs (see Figure 3), the M_w/M_n dependence of G_p is due to the amorphous morphology. The G_p is plotted against the fractions of the tie molecules connecting two, three or four lamellae in Figure 6. Although G_p was independent of the fraction of the tie molecules connecting two lamellar crystals, G_p increased with increasing the fractions of the tie molecules connecting three or more lamellae.

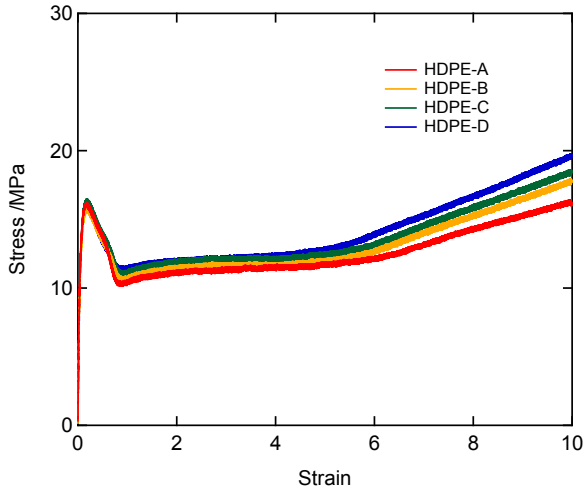

Figure 5. Stress–strain curves for all the samples at a strain rate of 0.5 min^{-1} and 25°C. All data of stress–strain curves are shown in Figure S3.

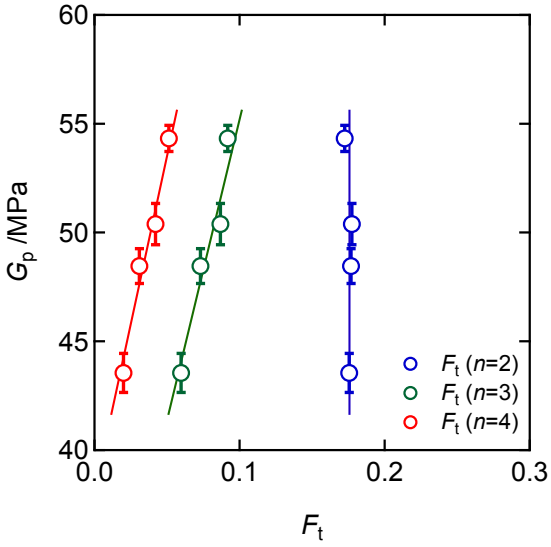

Figure 6. Fractions of tie molecules connecting two (blue), three (green), and four (red) lamellar crystals plotted against the strain-hardening modulus.

According to Haward–Thackray theory[68,69], the true stress is proportional to the Gaussian strain $\lambda^2-\lambda^{-1}$, where λ denotes the draw ratio, in the strain-hardening region, with the slope corresponding to the strain-hardening modulus G_p, which is related to the mechanical response of the deformed network structure. Considering that the tensile properties in the strain-hardening region are associated with the tensile deformation of the anisotropic fibrillar materials, G_p was precisely estimated from the reduced stress–strain curves in Figure 7(a) using the Gaussian strain normalized by the natural draw ratio λ_{ND}[69-71]:

$$\lambda\sigma = G_p\left[\left(\frac{\lambda}{\lambda_{ND}}\right)^2 - \frac{\lambda_{ND}}{\lambda}\right] + C, \tag{19}$$

where the intercept C corresponds to the necking stress. G_p can be assumed to be proportional to the network density ν as $G_p = \nu k_B T$, where k_B and T denote the Boltzmann's constant and temperature, respectively.[69,70] The conventional slope of the

strain-hardening region in the stress–strain curves (Figure 5) showed a negative dependence on temperature; however, the proportionality of the slope G_p with temperature was confirmed for various PE and PP materials.[70]

The network density determined from the experimental G_p is plotted against M_w/M_n in Figure 7(b). The network density linearly increased with increasing M_w/M_n, indicating that the HDPE samples with higher M_w/M_n had a stronger network structure. Considering that the lamellar crystalline morphology was unchanged for these HDPEs (see Figure 3), the amorphous morphology appears to mainly affect the network density. According to the results shown in Figure 7(b), tie molecules connecting three or more lamellar crystals mainly contributed to the strength of the network structure because the fraction of tie molecules connecting several lamellae increased with an increasing M_w/M_n (see Figure 6). Although the crystalline morphology of the present samples is essentially the same, the intercepts in Figure 7(a) slightly increases with M_w/M_n, suggesting enhancement of molecular orientation into the stretching direction.

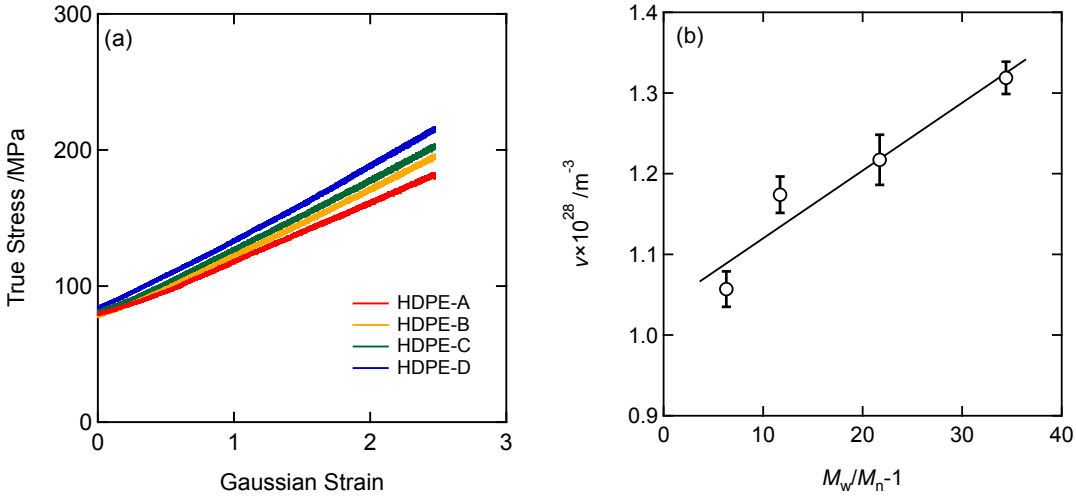

Figure 7. (a) The true stress plotted against the gaussian strain normalized by natural draw ratio for HDPEs and (b) polydispersity index dependence of the network density. All data of true stress–gaussian strain curves are shown in Figure S4.

According to Nitta-Takayanagi[12,65,72], the deformation units that govern the yielding behavior are not individual lamellar crystals but lamellar clusters composed of a few stacked lamellae. Considering that a molecule with an unperturbed dimension in the melt does not change in the solid state upon rapid crystallization[73], the exclusion process of chain ends causes the tie molecules to bind several stacked lamellae and produces units with a single Gaussian chain size including many intertwining chains. When the cubic units thus solidified develop into the lamellar clusters forming spherulites, some extended tie molecules extending beyond the Gaussian chain size connect the adjacent lamellar clusters, leading to a network structure. The intercluster links (ICLs) are randomly and homogeneously dispersed in the spherulitic matrix and the network structure is embedded in the spherulites in the undeformed state.[12,65] Then, the ICLs support the external force, and their tractive forces act on the lamellar cluster surface, leading to fragmentation of the lamellar clusters into cluster units at the yield point and their rotation toward the stretching direction. The rearrangement of cluster units connected with ICLs gives the texture of necking. It follows that a combination of the ordering process of the ICLs (an attractive effect) and the exclusion process between the bulky cluster units (a repulsive effect) leads to a large-scale morphological transformation from an isotropic spherulitic structure to an ordered necked structure.[64,74] This view has been accepted and supported indirectly by mechanical data[12,65] as well as neutron scattering data[73,75]. The direct evidence of the existence of ICL networks in melt-crystallized PE spherulites was first demonstrated in an electron microscopy study performed by Keith-Padden et al.[76,77] The stress–strain curves of these samples in the elastic, yielding, and neck-propagation regions were almost identical for all the HDPE samples. This result was likely observed because these HDPEs with similar M_w have a similar cluster unit size. In addition, the

strain-hardening can be considered to result from a mechanical response of networks composed of bulky cluster-unit junctions.

Although the Haward–Thackray[67] model has been applied to deduce the network characteristics for semi-crystalline polymers,[69,70,78] it is reported that this model can only be applied to the tensile deformation in the smaller to moderate strain region.[11] According to Tang *et al*,[20] the fibrillar structure is composed of the microfibrils and the slippage of these microfibrils is the dominant process of the deformation of the fibrillar structure. It follows that the discrepancy from the Haward–Thackray model in the strain-hardening region can be ascribed to the formation of the fibrillar structure composed of microfibrils. Therefore, the interfibrillar tie chains connecting the adjacent microfibrils can be explained to act as the stress transmitters in the strain-hardening region.[13,15,79,80] It is thus plausible that the increase of the fraction of the tie molecules connecting several lamellae leads to a larger number of the interfibrillar tie chains, resulting in higher strain-hardening modulus.

The strain dependences of the orientation parameter $\langle P_2 \rangle$ for HDPEs along with their stress–strain curves are shown in Figure 8, and the corresponding data of $\langle P_4 \rangle_{mp}$ (related to $\langle P_2 \rangle$ through Equations (10) and (11)) are shown in Figure S5 in Supporting Information. In the elastic region, orientation parameter remained practically zero, indicating random orientation. This random orientation in the elastic region for semi-crystalline polymers has been shown with IR and WAXD measurements.[22,27] Beyond the first yield (maximum) point, $\langle P_2 \rangle$ began to increase, suggesting the onset of the molecular orientation. Moreover, M_w/M_n dependence of the orientation parameter appeared beyond the second yielding (concave) point: the HDPEs with higher M_w/M_n showed higher values of the orientation parameter. In the strain-hardening region, $\langle P_2 \rangle$ gradually increased with

increasing strain before reaching constant values. Although the overall behaviors of the orientation parameter were quite similar to each other, a M_w/M_n dependence was clearly observed in the yielding and the strain-hardening region, with higher M_w/M_n samples exhibiting higher values of the orientation parameters.

The orientation parameter $\langle P_2 \rangle$ at $\varepsilon = 7$ is plotted against M_w/M_n in Figure 9. The value of $\langle P_2 \rangle$ linearly increased with increasing M_w/M_n. Considering that the yielding behavior of semi-crystalline polymers can be interpreted as the reorientation of the lamellar cluster units[67], the molecular orientation of the crystalline chains is strongly affected by the amounts of ICLs acting as stress transmitters between the lamellar clusters[12,65]. Because ICLs are formed by the high-molecular-weight molecular chains, for which the size of the Gaussian chain is larger than that of some lamellar crystals[12,65], the increase in M_w/M_n leads to increasing amounts of ICLs, resulting in enhancement of the molecular orientation.

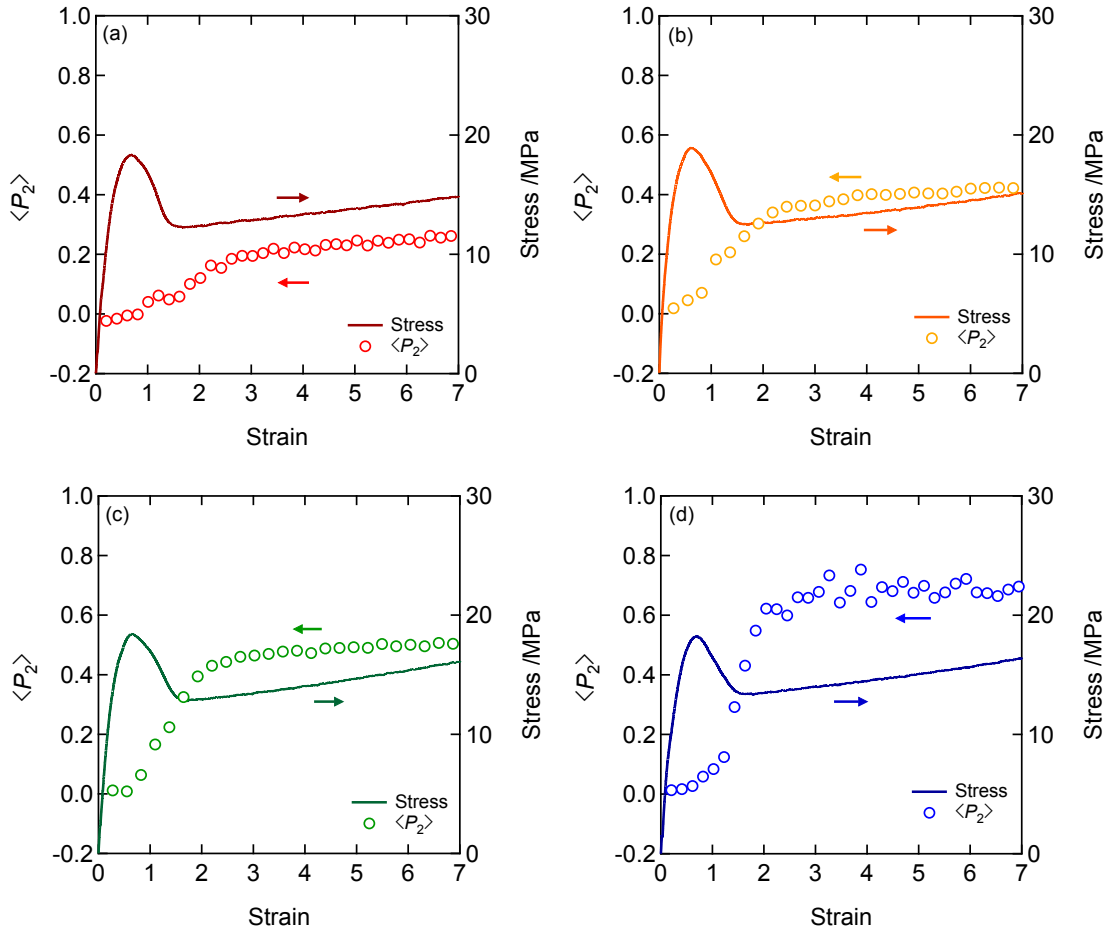

Figure 8. Strain dependences of the orientation parameters and stress–strain curves for (a) HDPE-A, (b) HDPE-B, (c) HDPE-C, and (d) HDPE-D. Strain dependences of $\langle P_4 \rangle_{mp}$ are shown in Figure S5.

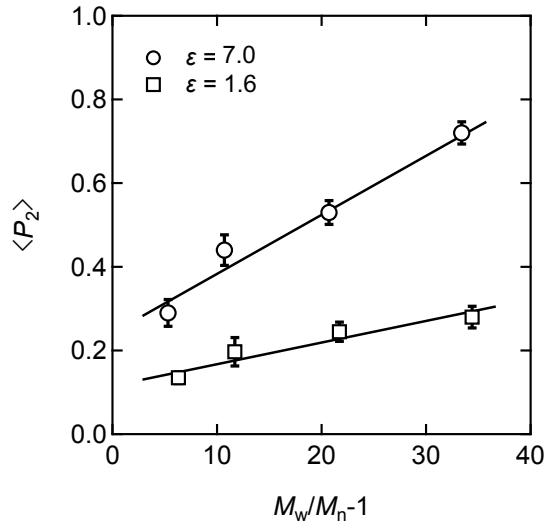

Figure 9. M_w/M_n dependence of the orientation parameter $\langle P_2 \rangle$ at $\varepsilon = 1.6$ and 7.0.

Figure 10 presents the stress–strain curve and the strain dependences of the mass fraction of the long consecutive trans chains and the orthorhombic crystallinity for HDPEs. The orthorhombic crystallinity remained almost constant, whereas the mass fraction of the long consecutive trans chains appreciably increased up to the first yield point for all the HDPEs. The increase in the mass fraction of the long consecutive trans chains indicates that the amorphous chains in the interlamellar layer are stretched within cluster units and that transformation from gauche to trans conformers is promoted. These findings are consistent with previous theoretical and experimental results indicating that the applied stress is mainly concentrated in the interlamellar amorphous phase in the elastic region.[45,81-83] Beyond the yielding region, the orthorhombic crystallinity decreased significantly to approximately 20% for all the HDPEs, whereas the fraction of the trans chains only slightly decreased in the yielding region. Note that the values of crystallinities obtained from WAXD patterns of the drawn specimens elongated up to $\varepsilon =$ 7.0 were similar to those for the undrawn specimen, as shown in Table S1 in the

Supporting Information. Similar structural changes under yielding have been reported in a Raman spectroscopic study on linear low-density PEs: the all-trans fraction increased with increasing strain, whereas the orthorhombic crystallinity drastically decreased beyond the yielding region.[51,84] Because the orthorhombic crystallinity obtained from Raman spectra is very sensitive to the perfection of crystalline regularity compared to those from WAXD and differential scanning calorimetry,[50] the drop of the orthorhombic crystallinity observed for the present samples suggests that distortion in the regularity of the orthorhombic crystalline structure occurs without conformational changes. According to the recent NMR and WAXD experiments, the distortion of the crystalline regularity is caused by the rotation of the molecular chain segments in the lamellar crystals under elongation.[14,85,86] Such crystalline distortion leads to the lowering of lattice symmetry of the orthorhombic crystalline cell with maintaining its lattice constants.[14] Thus, the decrease of the orthorhombic crystallinity in Figure 10 can be interpreted as strain-induced disordering of the crystalline structure without affecting the trans conformation. In the strain-hardening region, the orthorhombic crystallinity gradually increased with increasing strain and reached an asymptotic value, suggesting that the orthorhombic crystalline structure gradually recovers from the disordered states. However, the fraction of the long consecutive trans chains increased beyond the yielding region, and HDPE samples with higher M_w/M_n contained slightly higher fractions of long consecutive trans chains, as shown in Figure 11. These results suggest that the molecular chains in the amorphous phase are highly extended for HDPE samples with higher M_w/M_n, with the conversion from gauche to trans conformation under tension enhanced for higher M_w/M_n. Moreover, small-angle neutron scattering data[84] suggest that the longer molecular chains are more highly stretched in the uniaxial deformation of HDPE. Consequently, it is likely

that the higher fractions of long consecutive trans chains for HDPEs with higher M_w/M_n result from the elongation of the high-molecular-weight chains. This conclusion is consistent with the present results that the increase in the fraction of tie molecules connecting several lamellae due to the high-molecular-weight component leads to a stronger network structure.

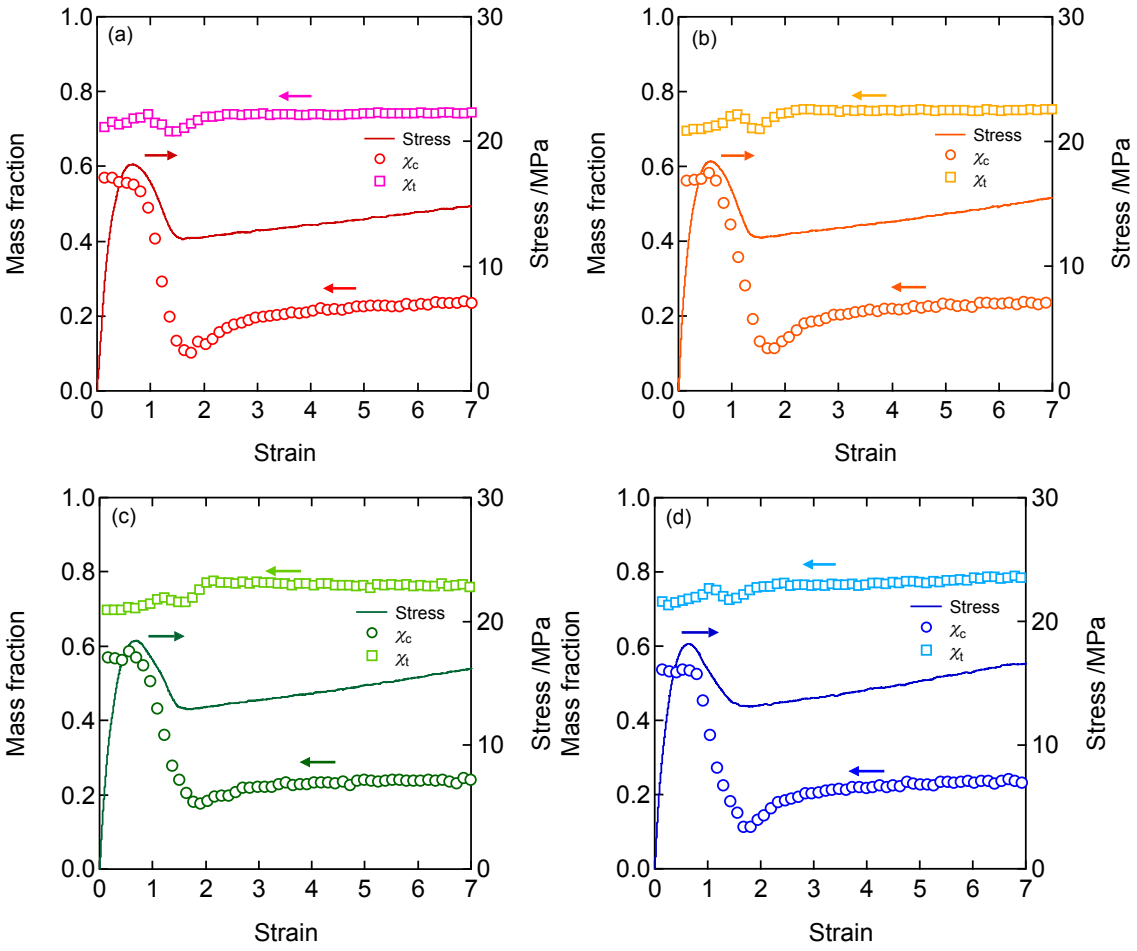

Figure 10. Strain dependences of the orthorhombic crystallinity and mass fraction of the long consecutive trans chains and stress–strain curves for (a) HDPE-A, (b) HDPE-B, (c) HDPE-C, and (d) HDPE-D.

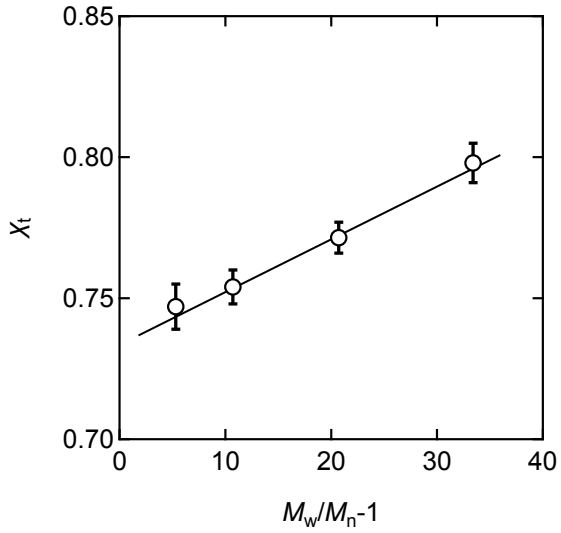

Figure 11. M_w/M_n dependence of the mass fraction of the long consecutive trans chains χ_t at $\varepsilon = 7$.

Schematic illustrations of the deformation of the HDPE are presented in Figure 12. Note that the lamellae oriented in the stretching direction were omitted to emphasize the effect of the polydispersity index. The size of the cluster units, which is determined by the averaged end-to-end distance of the chains, can be assumed to be almost constant because of the similar M_w. It follows that higher M_w/M_n samples contain larger fractions of tie molecules connecting several lamellae in the interlamellar amorphous layers within the lamellar cluster units. Beyond the yielding point, the several stacked lamellae forming spherulites are fragmented into the isometric several stacked lamellae as mobile units (namely, lamellar cluster units)[12,65,67] accompanied by disordering of the orthorhombic crystalline chains during the yielding deformation. The molecular orientation of the crystalline chains is suppressed by the excluded volume effects of the rigid and bulky lamellar cluster units, resulting in the oblique molecular orientation in the yielding region. The deformation mechanism under yielding is not affected by M_w/M_n because the

amorphous network of the tie molecules remains confined in the amorphous layers within the lamellar cluster units and is inactive. In the necking region beyond yielding, rearrangement of the cluster units in such a way that the crystalline chain axis orients in the stretching direction was observed for the HDPEs, with enhancement of the orientation for HDPEs with higher M_w/M_n. The enhancement of the orientation was induced by the increase in the number of intercluster links acting as stress transmitters between cluster units. Moreover, for HDPE samples with higher M_w/M_n, the fraction of long consecutive trans chains increases because the interlamellar tie molecules incorporated in the dense network are highly stretched under elongation. In the strain-hardening region, the lamellar cluster units are uniaxially deformed in the stretching direction, and the interlamellar amorphous chains become active. In particular, tie molecules connecting several lamellae are highly stretched and act as stress transmitters in the strain-hardening region. Thus, the fraction of tie molecules connecting several lamellae increases within the same-size lamellar cluster units with increasing M_w/M_n for a fixed M_w, resulting in a larger G_p.

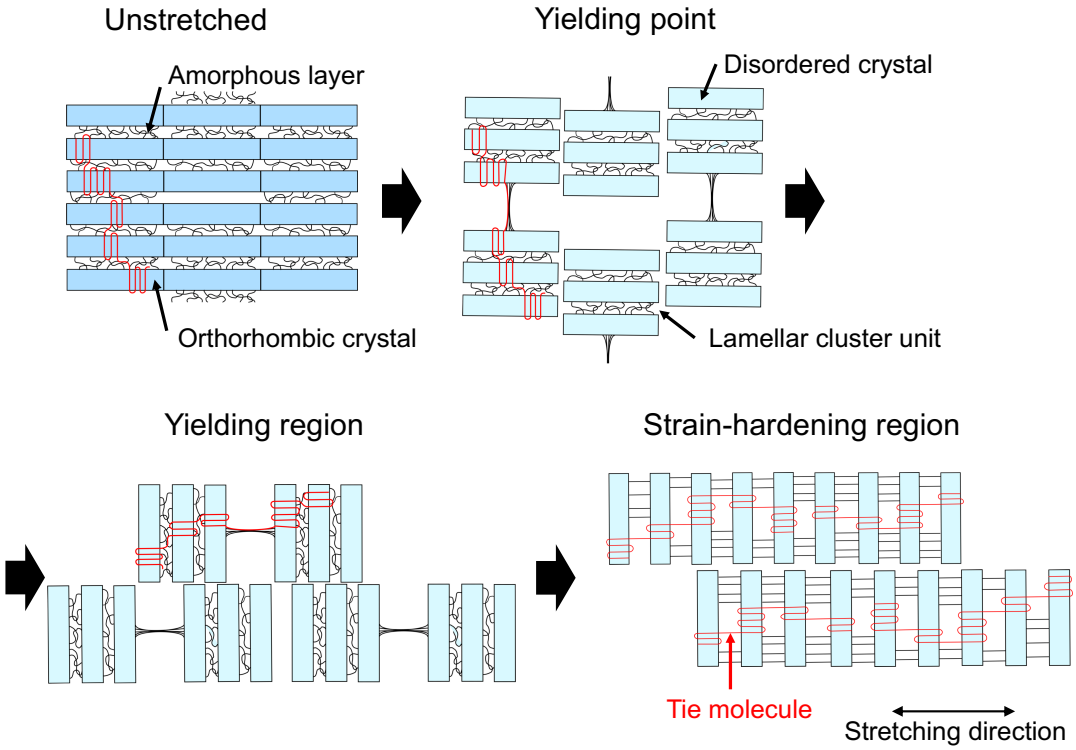

Figure 12. Deformation mechanism for uniaxial deformation of HDPE under uniaxial stretching process. The lamellae oriented perpendicular to the stretching direction before stretching are depicted.

5. Conclusions

The influences of M_w/M_n on the microscopic structure and deformation behaviors of HDPE under uniaxial stretching were investigated by simultaneously performing tensile tests and Raman spectroscopy for a set of HDPEs with fixed M_w and a wide range of M_w/M_n. Whereas lamellar crystalline morphology was essentially unaffected by M_w/M_n, the fraction of tie molecules connecting several lamellae increased with increasing M_w/M_n. Because the tie molecules are contained in the lamellar cluster unit in the elastic and yielding region, the M_w/M_n dependence is obvious only in the strain-hardening region as the increase of the network density. The increase of the tie molecules connecting several

lamellae leads to the enhancement of the molecular orientation because these tie molecules act as the intercluster links. Our experimental results provide new microscopic insights into the influences of M_w/M_n on the supermolecular structure and uniaxial deformation behavior of PE.

Author Information

Corresponding Author:

*E-mail: hiejima@se.kanazawa-u.ac.jp

ORCID

https://orcid.org/0000-0002-9494-3004 (Takumitsu Kida)

https://orcid.org/0000-0001-9197-2021 (Yusuke Hiejima)

https://orcid.org/0000-0002-1218-2935 (Koh-hei Nitta)

Notes

The authors declare no competing financial interest.

Acknowledgments

The authors would like to thank Prof. Yuko Amo (Yamagata University) for assistance with the low-frequency Raman spectroscopy measurements and analyses. The authors would also like to acknowledge Mr. Yuya Tsuchida (Northeastern Industrial Research Center of Shiga Prefecture) for assistance with the HT-GPC measurements. TK is grateful for financial support received from a Grant-in-Aid for JSPS Research Fellow 16J00528.

Supporting Information

Complementary plots: Correction factors for calculating crystallinity and fraction of long consecutive trans chains for stretched samples (Figure S1), Corrected values of crystallinity and the fraction of the long consecutive trans chains for stretched HDPE (Figure S2), Supplementary data of stress–strain curves for all HDPEs (Figure S3), Supplementary data of the true stress plotted against the gaussian strain for all HDPEs (Figure S4), Representative data of $\langle P_4 \rangle_{mp}$ as a function of strain for all HDPEs (Figure S5), Values of crystallinity of the undrawn and drawn HDPE samples obtained from WAXD (Table S1).

References

(1) Strobl, G. R. *The Physics of Polymers*; Springer: Berlin, 2013.

(2) Oleinik, E. F. Plasticity of Semicrystalline Flexible-Chain Polymers at the Microscopic and Mesoscopic Level. *Polymer Science. Series C* **2003**, *45*, 17–117.

(3) Gedde, U. W. *Polymer Physics*; Chapman & Hall: London, 1995.

(4) Seguela, R. *J.* Critical Review of the Molecular Topology of Semicrystalline Polymers: The Origin and Assessment of Intercrystalline Tie Molecules and Chain Entanglements. *Polym. Sci. B Polym. Phys.* **2005**, *43* (14), 1729–1748.

(5) Kennedy, M. A.; Peacock, A. J.; Mandelkern, L. Tensile Properties of Crystalline Polymers: Linear Polyethylene. *Macromolecules* **1994**, *27* (19), 5297–5310.

(6) Ward, I. M.; Sweeney, J. *Mechanical Properties of Solid Polymers, 3rd Edition*; John Wiley & Sons: London, 2013.

(7) Graham, J. T.; Alamo, R. G.; Mandelkern, L. The Effect of Molecular Weight and Crystallite Structure on Yielding in Ethylene Copolymers. *J. Polym. Sci. B Polym. Phys.* **1997**, *35* (2), 213–223.

(8) Colby, R. H.; Fetters, L. J.; Graessley, W. W. Melt Viscosity-Molecular Weight Relationship for Linear Polymers. *Macromolecules* **1987**, *20* (9), 2226–2237.

(9) Pearson, D. S.; Ver Strate, G.; Meerwall, Von, E.; Schilling, F. C. Viscosity and Self-Diffusion Coefficient of Linear Polyethylene. *Macromolecules* **1987**, *20* (5), 1133–1141.

(10) Onogi, S.; Masuda, T.; Kitagawa, K. Rheological Properties of Anionic Polystyrenes. I. Dynamic Viscoelasticity of Narrow-Distribution Polystyrenes. *Macromolecules* **1970**, *3* (2), 109–116.

(11) Hiss, R.; Hobeika, S.; Lynn, C.; Strobl, G. R. Network Stretching, Slip Processes, and Fragmentation of Crystallites during Uniaxial Drawing of Polyethylene and Related Copolymers. A Comparative Study. *Macromolecules* **1999**, *32* (13), 4390–4403.

(12) Nitta, K.-H.; Takayanagi, M. Novel Proposal of Lamellar Clustering Process for Elucidation of Tensile Yield Behavior of Linear Polyethylenes. *J. Macromol. Sci., Part B: Phys.* **2003**, *42* (1), 107–126.

(13) Lu, Y.; Men, Y. Cavitation-Induced Stress Whitening in Semi-Crystalline Polymers. *Macromol. Mater. Eng.* **2018**, *303* (11), 1800203.

(14) Wang, Z.; Liu, Y.; Liu, C.; Yang, J.; Li, L. Understanding structure-mechanics relationship of high density polyethylene based on stress induced lattice distortion. *Polymer* **2019**, *160*, 170–180.

(15) Lu, Y.; Wang, Y.; Chen, R.; Zhao, J.; Jiang, Z.; Men, Y. Cavitation in Isotactic Polypropylene at Large Strains during Tensile Deformation at Elevated Temperatures. *Macromolecules* **2015**, *48* (16), 5799–5806.

(16) Xiong, B.; Lame, O.; Chenal, J.-M.; Rochas, C.; Seguela, R.; Vigier, G. Temperature-Microstructure Mapping of the Initiation of the Plastic Deformation

Process in Polyethylene via In Situ WAXS and SAXS. *Macromolecules* **2015**, *48* (15), 5267–5275.

(17) Men, Y.; Rieger, J.; Strobl, G. R. Role of Entangled Amorphous Network in Tensile Deformation of Semicrystalline Polymers. *Phys. Rev. Lett.* **2003**, *91* (9), 095502.

(18) Zuo, F.; Keum, J. K.; Chen, X.; Hsiao, B. S.; Chen, H.; Lai, S.-Y.; Wevers, R.; Li, J. The role of interlamellar chain entanglement in deformation-induced structure changes during uniaxial stretching of isotactic polypropylene. *Polymer* **2007**, *48* (23), 6867–6880.

(19) Bower, D. I.; Maddams, W. F. *The Vibrational Spectroscopy of Polymers*; Cambridge University Press: New York, 1992.

(20) Tang, Y.; Jiang, Z.; Men, Y.; An, L.; Enderle, H.-F.; Lilge, D.; Roth, S. V.; Gehrke, R.; Rieger, J. Uniaxial deformation of overstretched polyethylene: In-situ synchrotron small angle X-ray scattering study. *Polymer* **2007**, *48* (17), 5125–5132.

(21) Jiang, Z.; Tang, Y.; Men, Y.; Enderle, H.-F.; Lilge, D.; Lilge, D.; Roth, S. V.; Gehrke, R.; Rieger, J. Structural Evolution of Tensile-Deformed High-Density Polyethylene during Annealing: Scanning Synchrotron Small-Angle X-ray Scattering Study. *Macromolecules* **2007**, *40* (20), 7263–7269.

(22) Jiang, Z.; Tang, Y.; Rieger, J.; Enderle, H.-F.; Lilge, D.; Roth, S. V.; Gehrke, R.; Wu, Z.; Li, Z.; Men, Y. Structural evolution of tensile deformed high-density polyethylene at elevated temperatures: Scanning synchrotron small- and wide-angle X-ray scattering studies. *Polymer* **2009**, *50* (16), 4101–4111.

(23) Wang, D.; Shao, C.; Zhao, B.; Bai, L.; Wang, X.; Yan, T.; Li, J.; Pan, G.; Li, L. Deformation-Induced Phase Transitions of Polyamide 12 at Different Temperatures: An in Situ Wide-Angle X-ray Scattering Study. *Macromolecules* **2010**, *43* (5), 2406–2412.

(24) Liu, Y.; Cui, K.; Tian, N.; Zhou, W.; Meng, L.; Li, L.; Ma, Z.; Wang, X. Stretch-Induced Crystal–Crystal Transition of Polybutene-1: An in Situ Synchrotron Radiation Wide-Angle X-ray Scattering Study. *Macromolecules* **2012**, *45* (6), 2764–2772.

(25) Qiao, Y.; Wang, H.; Men, Y. Retardance of Form II to Form I Transition in Polybutene-1 at Late Stage: A Proposal of a New Mechanism. *Macromolecules* **2018**, *51* (6), 2232–2239.

(26) Plass, M.; Streck, R.; Nieto, J.; Siesler, H. W. Rheo-optical FT-IR Spectroscopy of LLDPE: Effect of Comonomer and Composite Materials. *Macromol. Symp.*

2008, *265* (1), 166–177.

(27) Song, Y.; Nitta, K.-H.; Nemoto, N. Deformation Mechanisms of Polymer Thin Films by Simultaneous Kinetic Measurement of Microscopic Infrared Dichroism and Macroscopic Stress. 2. Molecular Orientation during Necking Process of Isotactic Polypropylene. *Macromolecules* **2003**, *36* (6), 1955–1961.

(28) Li, H.; Zhou, W.; Ji, Y.; Hong, Z.; Miao, B.; Li, X.; Zhang, J.; Qi, Z.; Wang, X.; Li, L.; Li, Z.-M. Spatial distribution of crystal orientation in neck propagation: An in-situ microscopic infrared imaging study on polyethylene. *Polymer* **2013**, *54* (2), 972–979.

(29) Nitta, K.-H.; Sawada, T.; Yoshida, S.; Kawamura, T. Three dimensional molecular orientation of isotactic polypropylene films under biaxial deformation at higher temperatures. *Polymer* **2015**, *74*, 30–37.

(30) Long, D. A. *Raman Spectroscopy*; MacGraw-Hill: New York, 1977.

(31) T Tanaka, M.; Young, R. J. Review Polarised Raman spectroscopy for the study of molecular orientation distributions in polymers. *J. Mater. Sci.* **2006**, *41* (3), 963–991.

(32) Bower, D. I. Investigation of Molecular Orientation Distributions by Polarized Raman Scattering and Polarized Fluorescence. *J. Polym. Sci. Polym. Phys. Ed.* **1972**, *10* (11), 2135–2153.

(33) Bower, D. I. Orientation Distribution Functions for Uniaxially Oriented Polymers. *J. Polym. Sci. Polym. Phys. Ed.* **1981**, *19* (1), 93–107.

(34) Štokr, J.; Schneider, B.; Doskočilová, D. Conformational structure of poly (ethylene terephthalate). Infra-red, Raman and nmr spectra. *Polymer* **1982**, *23*, 714–721.

(35) Naylor, C. C.; Kip, B. J.; Meier, R. J.; Kip, B. J.; Williams, K. P. J.; Conroy, N.; Gerrard, D. L.; Mason, S. M.; Gerrard, D. L. Raman Spectroscopy Employed for the Determination of the Intermediate Phase in Polyethylene. *Macromolecules* **1995**, *28* (8), 2969–2978.

(36) Meier, R. J. Studying the length of trans conformational sequences in polyethylene using Raman spectroscopy: a computational study. *Polymer* **2002**, *43*, 517–522.

(37) Migler, K. B.; Kotula, A. P.; Walker, A. R. H.; Hight Walker, A. R. Trans-Rich Structures in Early Stage Crystallization of Polyethylene. *Macromolecules* **2015**, *48* (13), 4555–4561.

(38) Kida, T.; Oku, T.; Hiejima, Y.; Nitta, K.-H. Deformation mechanism of high-density polyethylene probed by in situ Raman spectroscopy. *Polymer* **2015**, *58*,

88–95.

(39) Kida, T.; Hiejima, Y.; Nitta, K.-H. Rheo-optical Raman study of microscopic deformation in high-density polyethylene under hot drawing. *Polym. Test.* **2015**, *44*, 30–36.

(40) Kida, T.; Hiejima, Y.; Nitta, K.-H. Molecular orientation behavior of isotactic polypropylene under uniaxial stretching by rheo-Raman spectroscopy. *Express Polym. Lett.* **2016**, *10* (8), 701–709.

(41) Kida, T.; Hiejima, Y.; Nitta, K.-H. Rheo-Raman spectroscopic study of microscopic deformation behavior for ultra-low-density polyethylene. *Polym. Int.* **2018**, *67* (10), 1335–1340.

(42) Brandrup, J.; Immergut, E. H.; Grulke, E. A. *Polymer Handbook*; John Wiley & Sons: New York, 1999.

(43) Strobl, G. R.; Schneider, M. Direct evaluation of the electron density correlation function of partially crystalline polymers. *J. Polym. Sci. B Polym. Phys.* **1980**, *18* (6), 1343–1359.

(44) Huang, Y.-L.; Brown, N. The effect of molecular weight on slow crack growth in linear polyethylene homopolymers. *J. Mater. Sci.* **1988**, *23* (10), 3648–3655.

(45) Nitta, K.-H. A molecular theory of stress-strain relationship of spherulitic materials. *Comput. Theor. Polym. Sci.* **1999**, *9* (1), 19–26.

(46) Pigeon, M.; Prud'homme, R. E.; Pezolet, M. Characterization of Molecular Orientation in Polyethylene by Raman Spectroscopy. *Macromolecules* **1991**, *24* (20), 5687–5694.

(47) Frisk, N. S.; Ikeda, R. M.; Chase, D. B.; Rabolt, J. F. Determination of the Molecular Orientation of Poly(propylene terephthalate) Fibers Using Polarized Raman Spectroscopy: A Comparison of Methods. *Appl. Spectrosc.* **2004**, *58*, 279–286.

(48) Richard-Lacroix, M.; Pellerin, C. Accurate New Method for Molecular Orientation Quantification Using Polarized Raman Spectroscopy. *Macromolecules* **2013**, *46* (14), 5561–5569.

(49) Richard-Lacroix, M.; Pellerin, C. Novel Method for Quantifying Molecular Orientation by Polarized Raman Spectroscopy: A Comparative Simulations Study. *Appl. Spectrosc.* **2013**, *67* (4), 409–419.

(50) Strobl, G. R.; Hagedorn, W. Raman Spectroscopic Method for Determining the Crystallinity of Polyethylene. *J. Polym. Sci. B Polym. Phys.* **1978**, *16* (7), 1181–1193.

(51) Lagaron, J. M.; Dixon, N. M.; Reed, W.; Pastor, J. M.; Kip, B. J. Morphological

characterisation of the crystalline structure of cold- drawn HDPE used as a model material for the environmental stress cracking (ESC) phenomenon. *Polymer* **1999**, *40* (10), 2569–2586.

(52) Gall, M. J.; Hendra, P. J.; Peacock, C. J. Laser-Raman spectrum of polyethylene: Part 1. Structure and analysis of the polymer. *Polymer* **1972**, *13*, 104–108.

(53) Gall, M. J.; Hendra, P. J.; Peacock, O. J.; Cudby, M. E. A.; Willis, H. A. The laser-Raman spectrum of polyethylene: The assignment of the spectrum to fundamental modes of vibration. *Spectroshimica Acta Part A: Mol. Spectrosc.* **1972**, *28A*, 1485–1496.

(54) Voigt-Martin, I. G.; Stack, G. M.; Peacock, A. J.; Mandelkern, L. A comparison of the Raman LAM and electron microscopy in determining crystallite thickness distributions: Polyethylenes with narrow size distributions. *J. Polym. Sci. B Polym. Phys.* **1989**, *27* (5), 957–965.

(55) Kobayashi, M. Effects of interlamellar forces on longitudinal acoustic modes of n-alkanes. *J. Chem. Phys.* **1983**, *78* (11), 6391.

(56) Olf, H. G.; Peterlin, A. Laser-Raman Study of the Longitudinal Acoustic Mode in Polyethylene. *J. Polym. Sci. Polym. Phys. Ed.* **1974**, *12*, 359–384.

(57) Glotin, M.; Mandelkern, L.; Glotin, M. On the Use of Raman-Active Longitudinal Acoustic Modes in the Study of Polyethylene Lamellar Structures. *J. Polym. Sci. Polym. Phys. Ed.* **1983**, *21*, 29–43.

(58) Strobl, G. R.; Eckel, R. A Raman Spectroscopic Determination of the Interlamellar Forces in Crystalline *n*-Alkanes and of the Limiting Elastic Modulus E_c of Polyethylene. *J. Polym. Sci. Polym. Phys. Ed.* **1976**, *14* (5), 913–920.

(59) Amo, Y.; Tominaga, Y. Low-frequency Raman study of water isotopes. *Physica A* **2000**, *276*, 401–412.

(60) Voigt-Martin, I. G.; Mandelkern, L. Numerical analysis of lamellar thickness distributions. *J. Polym. Sci. B Polym. Phys.* **1989**, *27*, 967–991.

(61) Ward, I. M. *Structure and Properties of Oriented Polymers*; Chapman & Hall: London, 1975.

(62) Peterlin, A. Molecular Model of Drawing Polyethylene and Polypropylene. *J. Mater. Sci.* **1971**, *6*, 490–508.

(63) Seguela, R.; Rietsch, F. Double yield point in polyethylene under tensile loading. *J Mater Sci Lett* **1990**, *9* (1), 46–47.

(64) Nitta, K.-H.; Takayanagi, M. Application of Catastrophe Theory to the Neck-initiation of Semicrystalline Polymers Induced by the Intercluster Links. *Polym.*

J. **2006**, *38* (8), 757–766.

(65) Takayanagi, M.; Nitta, K.-H.; Kojima, O. Application of Lamellar Clustering Theory to Isotactic Polypropylene and Direct Observation of Lamellar Cluster Morphology by Electron Microscopy. *J. Macromol. Sci., Part B: Phys.* **2003**, *42* (5), 1049–1059.

(66) Seguela, R. On the Natural Draw Ratio of Semi-Crystalline Polymers: Review of the Mechanical, Physical and Molecular Aspects. *Macromol. Mater. Eng.* **2007**, *292* (3), 235–244.

(67) Kuriyagawa, M.; Nitta, K.-H. Structural explanation on natural draw ratio of metallocene-catalyzed high density polyethylene. *Polymer* **2011**, *52* (15), 3469–3477.

(68) Haward, R. N.; Thackray, G. The use of a mechanical model to describe isothermal stress-strain curves in glassy thermoplastics. *Proc. Roy. Soc. A* **1968**, *302*, 453–472.

(69) Haward, R. N. Strain Hardening of Thermoplastics. *Macromolecules* **1999**, *26* (22), 5860–5869.

(70) Haward, R. N. Strain Hardening of High Density Polyethylene. *J. Polym. Sci. B Polym. Phys.* **2007**, *45* (9), 1090–1099.

(71) Nitta, K.-H.; Yamana, M. Poisson's Ratio and Mechanical Nonlinearity Under Tensile Deformation in Crystalline Polymers. In *Rheology*; InTech: Rijeka, 2012.

(72) Nitta, K.-H.; Takayanagi, M. Role of tie molecules in the yielding deformation of isotactic polypropylene. *J. Polym. Sci. B Polym. Phys.* **1999**, *37* (4), 357–368.

(73) Fischer, E. W. Neutron Scattering Studies on the Crystallization of Polymers. *Polym. J.* **1985**, *17* (1), 307–320.

(74) Nitta, K.-H.; Kuriyagawa, M. Application of catastrophe theory to neck initiation of metallocene-catalyzed high-density polyethylene. *Polym. J.* **2011**, *44* (3), 245–251.

(75) Fischer, E. W.; Hahn, K.; Kugler, J.; Struth, U.; Born, R.; Stamm, M. An estimation of the number of tie molecules in semicrystalline polymers by means of neutron scattering. *J. Polym. Sci. Polym. Phys. Ed.* **1984**, *22* (8), 1491–1513.

(76) Keith, H. D.; Padden, F. J.; Vadimsky, R. G. Intercrystalline links in polyethylene crystallized from the melt. *J. Polym. Sci. Part A-2: Polym. Phys.* **1966**, *4* (2), 267–281.

(77) Keith, H. D.; Padden, F. J.; Vadimsky, R. G. Further Studies of Intercrystalline Links in Polyethylene. *J. Appl. Phys.* **1966**, *37* (11), 4027–4034.

(78) G'sell, C.; Jonas, J. J. Yield and transient effects during the plastic deformation

of solid polymers. *J. Mater. Sci.* **1981**, *16* (7), 1956–1974.

(79) Lu, Y.; Chen, R.; Zhao, J.; Jiang, Z.; Men, Y. Stretching Temperature Dependency of Fibrillation Process in Isotactic Polypropylene. *J. Phys. Chem. B* **2017**, *121* (28), 6969–6978.

(80) Xiong, B.; Lame, O.; Chenal, J. M.; Rochas, C.; Seguela, R. On the strain-induced fibrillar microstructure of polyethylene: Influence of chemical structure, initial morphology and draw temperature. *Express Polym. Lett.* **2016**, *10* (4), 311–323.

(81) Nitta, K.-H.; Takayanagi, M. Direct observation of the deformation of isolated huge spherulites in isotactic polypropylene. *J. Mater. Sci.* **2003**, *38* (24), 4889–4894.

(82) Xiong, B.; Lame, O.; Chenal, J.-M.; Rochas, C.; Seguela, R.; Vigier, G. In-situ SAXS study of the mesoscale deformation of polyethylene in the pre-yield strain domain: Influence of microstructure and temperature. *Polymer* **2014**, *55* (5), 1223–1227.

(83) Xiong, B.; Lame, O.; Chenal, J.-M.; Rochas, C.; Seguela, R.; Vigier, G. Amorphous Phase Modulus and Micro–Macro Scale Relationship in Polyethylene via *in Situ* SAXS and WAXS. *Macromolecules* **2015**, *48* (7), 2149–2160.

(84) López-Barrón, C. R.; Zeng, Y.; Schaefer, J. J.; Eberle, A. P. R.; Lodge, T. P.; Bates, F. S. Molecular Alignment in Polyethylene during Cold Drawing Using In-Situ SANS and Raman Spectroscopy. *Macromolecules* **2017**, *50* (9), 3627–3636.

(85) Li, Z.; Miyoshi, T.; Sen, M. K.; Koga, T.; Otsubo, A.; Kamimura, A. Solid-State NMR Characterization of the Chemical Defects and Physical Disorders in *a* Form of Isotactic Poly(propylene) Synthesized by Ziegler–Natta Catalysts. *Macromolecules* **2013**, *46* (16), 6507–6519.

(86) Kurz, R.; Achilles, A.; Chen, W.; Schäfer, M.; Seidlitz, A.; Golitsyn, Y.; Kressler, J.; Paul, W.; Hempel, G.; Miyoshi, T.; Thurn-Albrecht, T.; Saalwächter, K. Intracrystalline Jump Motion in Poly(ethylene oxide) Lamellae of Variable Thickness: A Comparison of NMR Methods. *Macromolecules* **2017**, *50* (10), 3890–3902.

Table of Contents

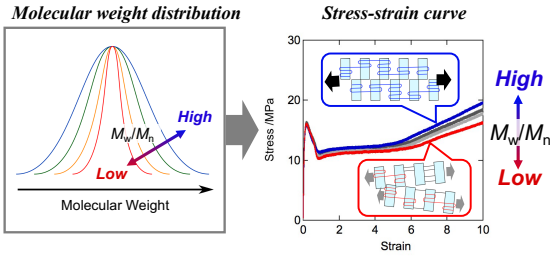

For Table of Contents Use Only

Rheo-Raman Spectroscopic Study on Uniaxial Deformation Behavior of High-Density Polyethylene Solids with Various Molecular Weight Distributions

Takumitsu Kida, Yusuke Hiejima, and Koh-hei Nitta